Theoretical Simulation and Experimental Verification of the Competition between Different Recombination Channels in GaN Semiconductor

Journal:	*Journal of Materials Chemistry C*
Manuscript ID	TC-ART-05-2022-002164.R1
Article Type:	Paper
Date Submitted by the Author:	29-Jul-2022
Complete List of Authors:	Zhang, Hai-Shan; Inner Mongolia University, Shi, Lin; Suzhou Institute of Nano-tech and Nano-bionics (SINANO), CAS, Liu, Zhenghui; Suzhou Institute of Nano-Tech and Nano-Bionics, Chinese Academy of Sciences, Xu, Gengzhao; Suzhou Institute of Nano-tech and Nano-bionics, Song, Wentao; Suzhou Institute of Nano-tech and Nano-bionics wang, ya-kun; Suzhou Institute of Nano-tech and Nano-Bionics Chinese Academy of Sciences xu, zhong-jie; Coll Optoelect Sci & Engn, National University of Defense Technology Yang, Xiaobao; South China University of Technology, Department of Phisics Zhao, Yujun; South China University of Technology, Physics Yang, Xuelin; Peking University, School of Physics Shen, Bo; Peking University School of Stomatology, Wang, Lin-Wang; Lawrence Berkeley National Laboratory, Xu, Ke; Suzhou Institute of Nano-tech and Nano-bionics (SINANO), CAS, Nano-characterization

Theoretical Simulation and Experimental Verification of the Competition between Different Recombination Channels in GaN Semiconductor

Hai-Shan Zhang,[1,2,3] Lin Shi,[2,4*] Zheng-Hui Liu,[2] Geng-Zhao Xu,[2] Wen-Tao Song,[2] Ya-Kun Wang,[2] Zhong-Jie Xu,[5] Xiao-Bao Yang,[3] Yu-Jun Zhao,[3] Xue-Lin Yang,[6] Bo Shen,[6] Lin-Wang Wang,[7,*] and Ke Xu[2,*]

[1]*School of Physical Science and Technology, Inner Mongolia University, Hohhot 010021, People's Republic of China*

[2]*Suzhou Institute of Nano-Tech and Nano-Bionics, Chinese Academy of Sciences, Suzhou 215123, People's Republic of China*

[3]*Department of Physics & Key Laboratory of Advanced Energy Storage Materials of Guangdong Province, South China University of Technology, Guangzhou 510640, People's Republic of China*

[4]*School of Materials Science and Engineering, Yancheng Institute of Technology, Yancheng 224051, PR China*

[5]*Coll Optoelect Sci & Engn, National University of Defense Technology, Changsha 410073, People's Republic of China*

[6]*State Key Laboratory of Artificial Microstructure and Mesoscopic Physics, School of Physics, Peking University, Beijing 100871, People's Republic of China*

[7]*Materials Sciences Division, Lawrence Berkeley National Laboratory, One Cyclotron Road, Mail Stop 66, Berkeley, California 94720, USA*

ABSTRACT

The dynamic competition of deep defect levels related to recombination processes is a crucial factor for a wide range of applications in semiconductors, however the time-resolved luminescence spectroscopies are very complex and challenging for clear explanations, and in time-resolved photoluminescence (TRPL) experiments, it is difficult for a single instrument to observe the decay processes across several orders of magnitude simultaneously. Based on the Shockley-Read-Hall (SRH) model, we present a method to simulate the defects-related TRPL processes in time scales ranging from picosecond to millisecond scale. Our approach considers the competition among the band edge and defects-related radiative and nonradiative recombination channels. In an *n*-type GaN sample, we demonstrate that following a pulse laser excitation, the substitutional defect C_N related yellow luminescence (YL) exhibits a double-exponential decay. The fast decay on the hundreds of the picoseconds is due to the band edge emission (BE), while the well-known slow decay at the microseconds is induced by electron relaxation from the conduction band to the defect state. The fast and slow decay lifetimes of YL in verification experiments are all in good agreement with our simulated results. This work provides an explicit physical picture of defect-related luminescence and the competition of different recombination channels in GaN.

Ⅰ. INTRODUCTION

Wide-bandgap semiconductors (WBGS) are widely used as the transducers,[1] light-emitting diodes (LED),[2] high electron mobility transistors (HEMT)[3, 4] and other applications owing to their large bandgaps, large piezoelectric effects and high breakdown voltages. The deep impurity levels often exist in WBGS, and they can be an optical center or a thermal center. Several experimental techniques are currently used to detect and quantify the point defects in WBGS. The deep-level transient spectroscopy (DLTS) can detect the carriers-capture cross section of the point defects with low concentrations.[5, 6] Positron annihilation spectroscopy (PAS) is efficient in detecting negatively charged defects, especially the cation vacancies.[7] Electron paramagnetic resonance (EPR) spectra can effectively detect the defect level position in semiconductors.[8] One of the most popular tools to explore point defects is photoluminescence (PL). In principle, it can be used to detect point defects with both shallow and deep energy levels and determine their concentrations, charge states, the strength of electron–phonon coupling *et al.*[9-11]

Time-resolved photoluminescence (TRPL) is a widely used spectroscopic technique in the physical characterization of semiconductors, which can provide time-dependent carrier dynamics and recombination information.[12] Although rich in its information, understanding the internal mechanism of the TRPL measurement has faced a big challenge due to the complicated competition between different channels. For *n*-type GaN, there are many publications about the most famous defect-related yellow luminescence (YL), and the corresponding decay lifetimes in different reports range from picoseconds[13] to microseconds.[14, 15] H. Haag and his co-workers proposed that the various lifetimes of YL in GaN measured by different experiments may arise from diverse excitation intensities and associated detection systems[13]. R. Y. Korotkov and J. Mickevicius proposed that the lifetimes of different magnitudes of YL are derived from different luminescence mechanisms.[16, 17] Furthermore, they hypothesized that the very fast decay observed under high excitation levels is related to the exciton band tail, but no detailed evidence and explanation were provided. All these show the current gap in the understanding of the defect-related TRPL processes.

In view of the current situation, a more detailed microscopic understanding of the TRPL is urgently needed, which should take into account competition between different channels. However, the competition among the recombination channels related to deep impurity levels is complicated, and the lack of theories to understand this has obstructed the application of WBGS. M. A. Reshchikov and co-workers employed a useful phenomenological model to describe the decays of defect-related yellow, red, green and blue luminescence in GaN.[18-21] In their work, only the decay on the microsecond scales of YL was presented, and the decay lifetime in the picosecond scales reported in Ref. 13 is not mentioned. Moreover, some of the key parameters in their model are derived from the fitting of experimental results. As we know, the experimental samples contain a variety of defect centers, and the fitted parameters actually contain the combined effects of multiple defect centers. Herein, we aim to map in detail the competitive processes between the specific defect-related YL and the intrinsic BE recombination channels over a long-time range. More importantly, instead of using fitting parameters as in the phenomenological model, we adopted *ab initio* calculated channel rates, including radiative decay and thermal nonradiative decay rates. This has significantly reduced the uncertainty in our prediction. Heyd–Scuseria–Ernzerhof (HSE) hybrid density functional theory[22, 23] is used to provide accurate electronic structures of point defects.[10, 24, 25] Several methods have been used to describe the defects related nonradiative recombination (NRR) process.[25-28] As shown in our previous works,[25, 28] the static coupling theory as implemented in PWmat[29, 30] can provide accurate results for the NRR process in point defects of III–V compounds. Based on the Fermi's Gold rule, we can also calculate the radiative recombination (RR) coefficient between different energy levels.[31, 32] Following these *ab initio* calculations, the carrier dynamics and the defect-related TRPL process can be directly simulated without any fitting parameters.

This paper is organized as follows. The theoretical model of TRPL is described in Section II. We give the details of simulated results and discussion of YL decay in Section III. In Section IV, we outline the experimental verification for the simulated fast and slow decay processes of YL, respectively. Section V concludes the paper.

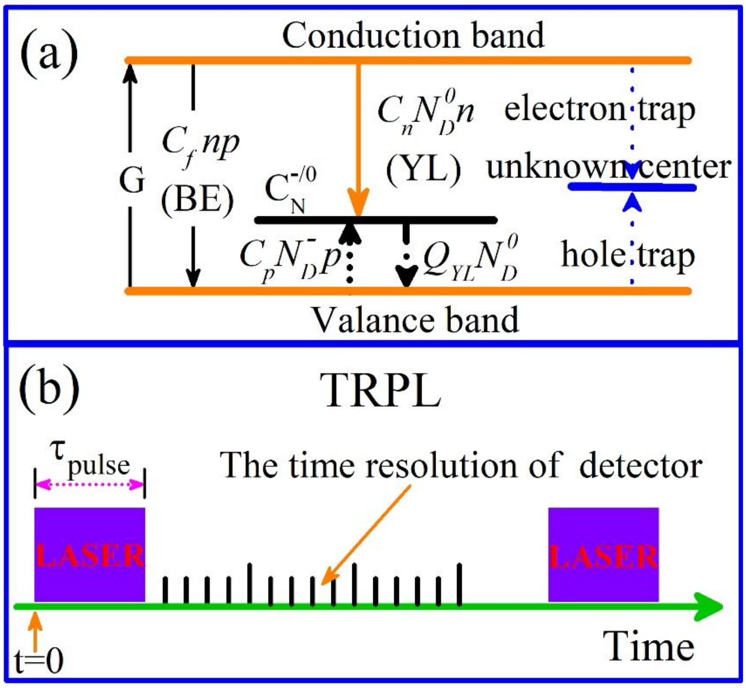

FIG. 1. Diagram to show the relevant excitation and recombination processes in GaN containing YL (a), and the simulated TRPL process (b). The radiative recombination, nonradiative recombination and thermal excited processes are indicated by solid line, black dot line and black dash dot, respectively. The unknown deep center-related recombination processes are indicated by blue dot line. The time zero (t=0) of our simulation process is labeled in (b).

Ⅱ. Theoretical model of TRPL

In this paper, we use the dynamic competition between defect-related YL and intrinsic BE emission in an *n*-type GaN as an example to illustrate this approach. As shown in Fig. 1(a), under an excitation of pulsed laser light (G), the non-equilibrium electron and hole are generated in the conduction and valance bands, respectively, followed by some carrier transitions associated with band edges and defect centers. Fig. 1(b) is a simplified schematic diagram of the TRPL process, and the pulse excitation starts at t=0. The horizontal axis range of the black vertical lines corresponds to the range of the

TRPL light detection system in the experiment, and the distance between the two adjacent black vertical lines corresponds to the resolution of the detection system. It is well known that the internal quantum efficiency of GaN samples grown on Si substrates used in our work is very low, which is due to some defects such as grain boundaries and stacking faults in the sample can become nonradiative recombination centers. It will introduce the unknown defect states into the bandgap and reduce the lifetime of minority carriers. Yutaka et al. listed several carrier capture centers in *n*-type GaN samples grown on Si substrate and confirmed that the most important hole capture center was the H1 center (The energy levels are about 0.86 eV~0.88 eV above the valence band maximum), which was responsible for the YL in GaN. In addition, the average concentration of the H1 center (4.2×10^{16} cm^{-3}) is three orders of magnitude higher than the average concentration of the main electron capture center (4.9×10^{13} cm^{-3}).[33] To further determine the recombination channels in our model, the room temperature-steady-state PL tests were carried out in advance. As shown in Fig. 2, our BE emission with the maximum at 3.40 eV and YL emission with the maximum at 2.20 eV are well separated (actually separated by a weak BL emission peak). By integrating the region of the spectrum, it can be seen that the intensity of BL only accounted for 7.7% of the total PL intensity at 285 K. Since at this stage, the exact nature of the BL is not well known, and we will ignore it to simplify our model. In our later TRPL experiment, the monochromator has a focal length of 550 mm and a grating groove line density of 1500 lines/mm, which can filter out the near-band-edge emission perfectly. In addition, for samples without YL emission, we cannot detect any spectral signal at the same YL wavelength. This proves that the YL we measured comes from a defect and not stray light. It is widely believed that the origin of the carbon-related YL in GaN is associated with C_N or C_N+O_N defects, and the defect level for the carbon-related defect is at about 0.7 eV above the valence band maximum (VBM).[8] In our recent work,[34] local vibrational modes (LVMs) of isolated C_N in C doped GaN samples are directly observed by performing Fourier Transform infrared spectroscopy and Raman scattering experiments. However, the LVMs of C_N+O_N are not observed even in the highest C doped samples (~10^{20} cm^{-3}), which demonstrates that the transition between "-" and "0" charge states of C_N defect is responsible for the YL in our C doped GaN samples. The concentrations of C impurity in our samples used in later TRPL experiments are as high as 7×10^{17} cm^{-3}, which are much higher than the concentration of carrier capture centers reported in Ref. 33. Therefore, the unknown carrier capture centers are ignored in our model, and only the competition between YL center (including radiative and nonradiative recombination channels) and band-edge recombination channels are considered.

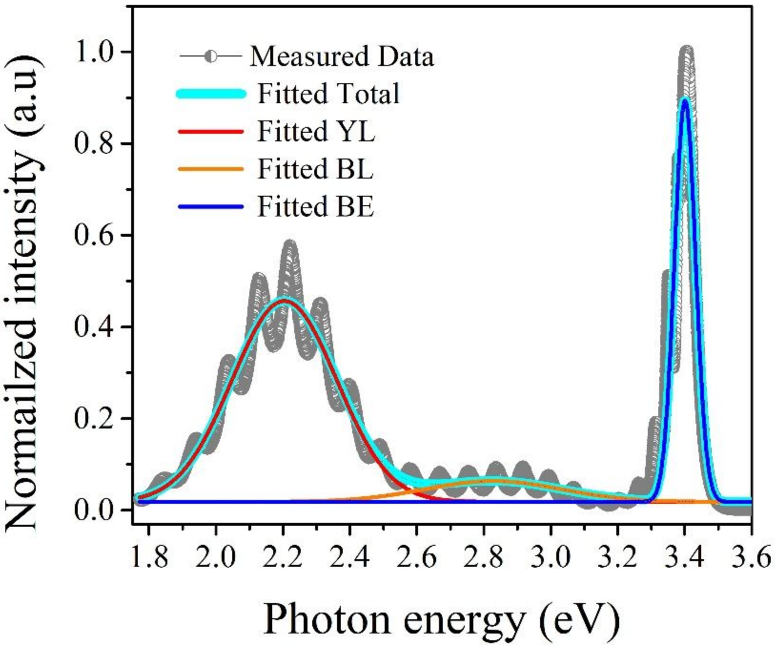

FIG. 2. Steady-state PL results of the sample N-836 that we used in later TRPL experiments were measured at 285 K. The solid lines are calculated using Gauss model $y = y_0 + (A/(w\times\sqrt{\pi/2}))\times\exp(-2\times((x-xc)/w)^2)$, with the following parameters: y_0=0.02; xc=2.20; w=0.31; A=0.17 for the YL band; y_0=0.02; xc =2.83; w =0.41; A=0.02 for the BL band; y_0=0.02; xc =3.40; w =0.06; A=0.07 for the BE band.

In present work, a 128-atom (4 × 4 × 2) supercell is used to calculate the transition levels of C_N defect by Vienna *ab initio* simulation package (VASP) code.[35, 36] Both the undoped and doped GaN atomic structures were optimized with the mesh of a 1 × 1 × 1 k-point grid by using the screened [22, 23] functional of HSE. As in a previous paper,[25] the mixing parameter (α) of HSE was set to 0.30. A kinetic energy cutoff of 450 eV was used in all calculations, and the force criteria were 0.001 eVÅ^{-1}. The calculated YL-related "−/0" transition energy of C_N is at 0.79 eV above the VBM. As shown in Fig. 1(a), the electron transition from conduction band to valence band corresponds to the BE emission with the RR rate of $C_f np$ (RR_{BE}).[37] Here, C_f is the RR coefficient for BE. n and p are the concentrations of free electrons and holes, respectively. The holes in the valence band can be captured nonradiatively by the negatively charged C_N^- defect state, and change it to neutral state C_N^0. The calculated RR coefficient of this process in our previous work is very small, about 10^{-14} cm^3 s^{-1}.[25] It means that this transition must be phonon related, and the NRR rate is $C_p N_D^- p$ (NRR_{YL}),[37] where N_D^- is the negative defect state concentration. The energy difference between the defect level and the conduction band is up to 2.71 eV (E_{Gap}-0.79), while the energies of phonons are basically less than 100 meV.[25] Using the static coupling method, we can get the phonon-assisted NRR coefficient of the electrons located in the conduction band falling to the neutral impurity at room temperature is about 10^{-64} cm^{3}s^{-1}, much less than the RR coefficient of this process (~10^{-13} cm^{3}s^{-1}). So this transition is independent of phonons, and YL will be released. The electrons RR rate is $C_n N_D^0 n$ (RR_{YL}),[37] and N_D^0 is the neutral defect concentration. C_p and C_n are the hole NRR and electron RR coefficients for the above two processes. $Q_{YL} N_D^0$ is the hole thermal transition rate from impurity level to valence band maximum (VBM), and the coefficient Q_{YL} is related to the C_p through a detail balance:[38]

$$Q_{YL} = C_p N_v g^{-1} \exp\left(-\frac{\Delta E}{kT}\right)$$

with

$$N_v = 2\left(\frac{m_h k_B T}{2\pi\hbar^2}\right)^{3/2}$$

Where C_p is the hole nonradiative recombination coefficient of the YL center, g is the degeneracy factor of the acceptor level, N_v is the effective density of states in the valence band, ΔE is the transition energy, m_h is the effective mass of the holes in the valence band.

As shown in Fig. 1(b), the whole TRPL process contains the pulse photoexcitation duration ($0 < t \le \tau_{\text{pulse}}$) and the duration after the laser pulse ($t > \tau_{\text{pulse}}$). The generation rate of photo-generated carriers ($\frac{dn_G}{dt}$ and $\frac{dp_G}{dt}$) during and after the laser pulse can be calculated as:[39]

$$\frac{dn_G}{dt} = \frac{dp_G}{dt} = \begin{cases} \int_0^{L_{\max}} \frac{\alpha(\lambda) I_0 e^{-\alpha(\lambda)L}}{\frac{hc}{\lambda} L_{\max}} dL, & 0 < t \le \tau_{\text{pulse}} \\ 0, & t > \tau_{\text{pulse}} \end{cases} \quad (1)$$

where λ is the wavelength of the excitation light, $\alpha(\lambda)$ is the absorption coefficients of the GaN layer, I_0 is the excitation light power density, h is Planck's constant, c is light velocity, and L_{max} is the effective thickness of the GaN absorber layer. Note, we take the assumption that the photo-generated carriers are well equilibrated spatially before different transitions. Thus, there is no need to solve spatial diffusion equations.

In our TRPL simulation, by referring to Fig. 1(a), the rate of change of the hole concentration in the valence band can be expressed as:

$$\frac{dp}{dt} = \frac{dp_G}{dt} - C_f np - C_p p N_D^- + Q_{YL} N_D^0 \quad (2)$$

Similarly, the rate of change of the electron concentration in the conduction band is expressed as:

$$\frac{dn}{dt} = \frac{dn_G}{dt} - C_f np - C_n n N_D^0 \quad (3)$$

The concentration of the charged YL related defect needs to satisfy the following equation:

$$\frac{dN_D^-}{dt} = -C_p p N_D^- + C_n n N_D^0 + Q_{YL} N_D^0 \quad (4)$$

Since we have an *n*-type GaN system, if we define the time at which the pulse excitation begins as $t = 0$, the Eqs. (2), (3) and (4) should satisfy initial conditions $n(0) = n_0$, $p(0) = 0$, $N_D^-(0) = N_D$ and $N_D^0(0) = 0$. By numerical calculation, we can figure out the time-resolved concentrations of n, p, N_D^- and N_D^0 by solving simultaneous Eqs.(2), (3) and (4). Thus, the time-resolved YL can be obtained. Note, in order to simplify the model, we ignore the transition of the carrier from the impurity level to the conduction band under photoexcitation, because whether this process is considered will not affect the decay process of YL. The explanation will be given in section Ⅲ.

Ⅲ. Results and Discussion

In our TRPL simulation, because it aims to explore the decay of YL in the order of picoseconds and microseconds, at least a femtosecond pulsed light source should be used. In order to be consistent with the light source used in the following experiment, the pulse width of the 266 nm pulse photoexcitation is 180 fs, and the peak power density is 4.34×10^{7} W /cm^{2} in the simulation. Because the pulse width is much shorter than the carrier recombination time to be considered in this paper, we can ignore the carrier recombination during the laser pulse. The absorption coefficient (1.77×10^{5} cm^{-1} at 266 nm) [40] we used indicates that the incident depth of the photoexcitation is about 57 nm. Moreover, we can get the diffusion length of the hole by the formula $L=\sqrt{D\tau}$, where D is the diffusivity, and τ is the total lifetime of the hole. D equals to $k_BT\mu/e$, where k_B is the Boltzman constant, T is temperature, μ is the mobility. The total lifetime of the hole needs to be satisfied $\tau^{-1}={\tau_0}^{-1}+{\tau_{def}}^{-1}$. τ_0 is the lifetime of the hole without the defect related recombination, and τ_{def} is the lifetime of the hole in the defect related recombination processes. In our work, the mobility of the hole was set as $\mu=23\ cm^2/Vs$ according to the Ref. [41]. The lifetimes τ_0 and τ_{def} in our sample correspond to the two decay lifetimes of BE in the TRPL experiment later, which are 1.96×10^{-10} s and 1.05×10^{-11} s, respectively. The above parameters are substituted into the equation ($L=\sqrt{D\tau}=\sqrt{(k_BT\mu/e)\tau}$), and we can obtain the diffusion length of the hole is about 24 nm, similar scale as the light absorption length. Thus, by refereeing to Ref. 38, we can assume the carries are roughly equilibrium spatially within 100 nm during the decay period of the hole. During this period and within this 100 nm, the originally negatively charged defects will be converted to neutrally charged defects. When the hole carrier has been depleted, the slow decay mechanism of YL happen between the free electron and the neutrally charged defects. Since the neutrally charged defects are immobile and frozen in space, this effectively limits the process in the slow second decay period within the 100 nm region. Thus, we assume that the absorption and recombination of photons are all within the effective depth of 100 nm, and the carriers are evenly distributed within this depth. In addition, Table I lists the above critical parameters (C_f, C_p and C_n) calculated by *ab initio* methods in our previous work.[25] The intrinsic *n*-type free electron concentration (n_0) before excitation for our simulated sample is 4.5 × 10^{17} cm^{-3} (Corresponding to the intrinsic electron concentration in our later N-836 experimental sample). The effective density of states N_v is $3.2\times10^{15}T^{3/2}$ cm^{-3} according to Ref. 18. It is difficult to directly determine the concentrations of YL center. In the TRPL experiment later in this paper, the BE luminescence shows a double exponential decay with lifetimes of 1.96×10^{-10} s and 1.05×10^{-11} s, respectively. Obviously, the 1.96×10^{-10} s lifetime is caused by the direct transition from CBM to VBM ($1/C_f\times n$), while the 1.05×10^{-11} s lifetime is caused by the depletion of non-equilibrium holes of all nonradiative recombination channels, including the YL and other unknown centers. In our model, the nonradiative recombination rate of the YL center is calculated by first-principles, and a YL center concentration satisfying the condition ($1/C_p\times N_D=1.05\times10^{-11}\,\mathrm{s}$) is employed.

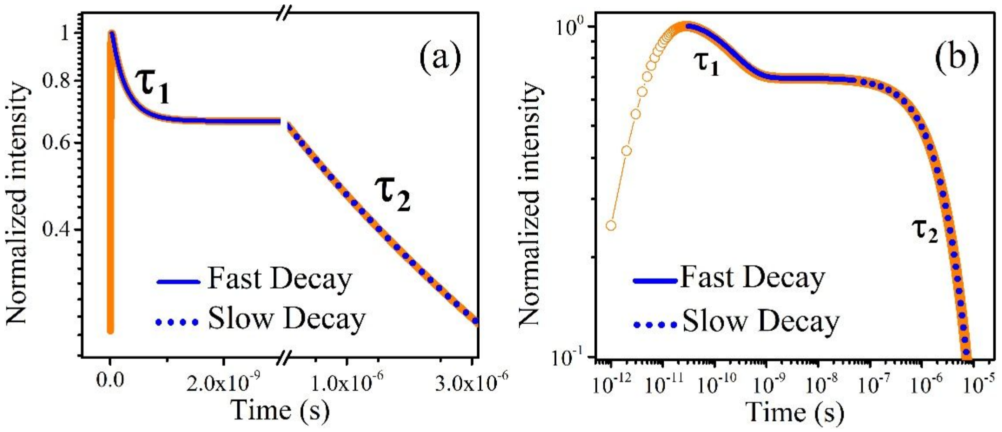

FIG. 3. The simulated time-resolved I_{YL} where the horizontal time axises are in linear (a) and logarithmic (b) scales. The fast (τ_1) and slow (τ_2) decays are shown as blue solid and dotted lines, respectively. Note, the horizontal axis in (a) has been divided into two regions, both are in linear scale, but dramatically different scaling factor.

The above parameters are substituted into Eq. (1), and we can get the photo-generated electron and hole concentrations ($n_G = p_G = 8.68\times10^{17}$ cm^{-3}) at end of the pulse. By solving simultaneous Eqs. (2), (3) and (4), we can get the time-resolved I_{YL}, and the results are shown in Fig. 3. In addition, the time-resolved n, p, N_D^-, N_D^0, RR_{BE} and RR_{YL} are shown in Figs. 4(a)-4(c). In the whole simulation, the time steps dt are set to 1 ps. Note, in order to show both the fast and slow exponential decay processes in the same figure, Fig. 3(a) is divided into two regions. Both of their horizontal scales are linear, and the vertical scales are logarithmic. Meanwhile, the whole curve can be represented in a different plot with a logarithm scale for the time t, and it is shown in Fig. 3(b). Obviously, the intensity of YL will increase first, then gradually shows a very obvious double-exponential decay, and the fitted fast and slow decay lifetimes are τ_1=2.48×10^{-10} s and τ_2=2.92×10^{-6} s, respectively.

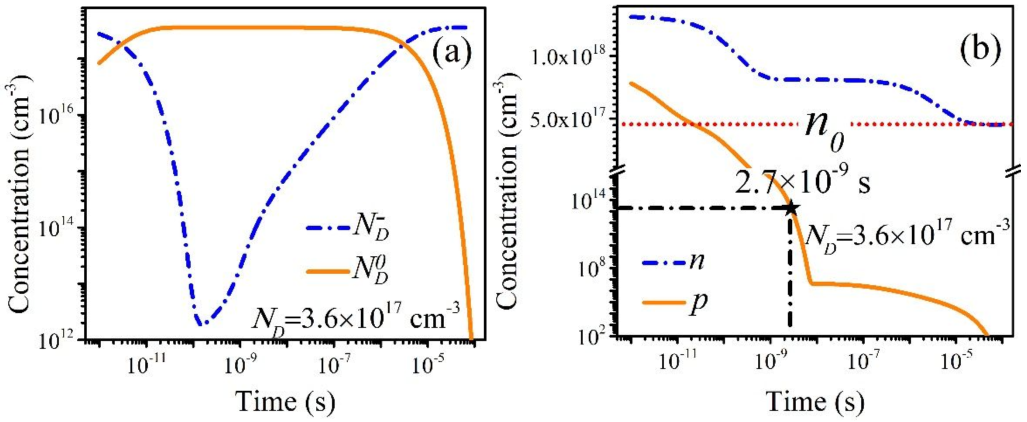

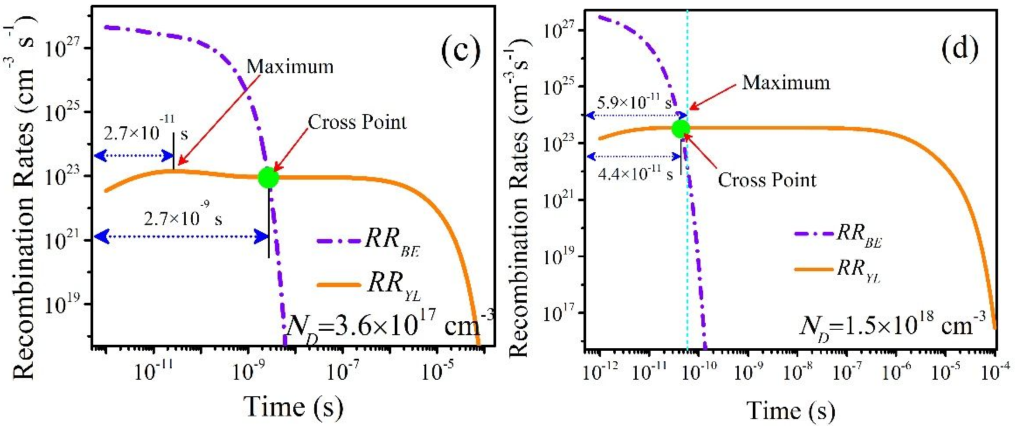

FIG. 4. The simulated time-resolved N_D^-, N_D^0 (a) and n, p (b) when the defect concentration is 3.6×10^{17} cm^{-3}. In (b), the intrinsic electron concentration n_0 is indicated by a red horizontal dotted line. The simulated time-resolved RR_{BE} and RR_{YL} rates when the defect concentrations are 3.6×10^{17} cm^{-3} (c) and 1.5×10^{18} cm^{-3} (d), respectively. In (c) and (d), the maximums of RR_{YL} and the cross points of RR_{YL} and RR_{BE} are labeled. Note, all the horizontal axises are in logarithmic scale.

The initial rise and the later double stage exponential decays of the YL intensity are the results of competition between different recombination channels. In the *n*-type semiconductor that contains deep defect levels like the model in Fig. 1(a), the impurity levels are all occupied at “-” charge state at the initial time (as shown in Fig. 4(a)). Corresponding to our experiment, the injection is large, and after the pulsed laser excitation, the total concentration of the electron is appreciably bigger than the original intrinsic *n*-type carrier concentration n_0. We assume that the defects are all in “-” charge state when the pulse stops. The intensity of YL is proportional to the product of n and N_D^0. Because the NRR rate of the hole jumping up to the defect is much faster than the RR rate of the electron relaxation down to the defect, the concentration of the neutral charge state defect N_D^0 increases immediately after light excitation (as shown in Fig. 4(a)), which corresponds to the initial steep increase of YL before 2.7×10^{11} s as shown in Fig. 4(c). As mentioned in Section Ⅱ, the photoionization of electrons from impurity level into the conduction band during the laser pulse is ignored, which is due to the transition rate of an electron from C_N^- to conduction band is much larger than the transition rate from valence band to conduction band. Even if the photoionization of electrons from the impurity level into the conduction band is taken into account in our model, part of C_N^- defects will change to C_N^0 under light excitation. When the pulse stops, the remaining "-" charge state defects will also be rapidly changed to "0" charge state due to NRR process. Therefore, whether the photoionization of electrons from the impurity level into the conduction band is considered will only slightly affect the rising process of YL, and have no effect on the decay process of YL. After this initial increase of YL, there is a fast decay period until about 2.7×10^{-9} s. As will be shown in Fig. 4(c), during this period, the BE decay rate (RR_{BE}, the second term in Eq.(3)) is much larger than the YL decay rate (RR_{YL}, the third term in Eq.(3)). Meanwhile, as shown in Figs. 4(a) and (b), during this period, the N_D^0 is essentially constant (N_D) while the electron concentration n decreases from $n_0 + n_G$ to $n_0 + N_D$. Thus, the first YL fast decay is dominated by the decreasing of n cause by BE recombination. Note, this decay period is not a pure exponential. Rather the decay for n is like: $n(t) = (n_G - N_D)\times\exp(-t/\tau_1) + n_0 + N_D$. At the end of this period, due to RR_{BE} and the nonradiative recombination process, the hole carrier has been depleted (as shown in Fig. 4(b)). Because of this, the overall RR_{BE} rate has dropped significantly and becomes smaller than the YL RR rate between electron and neutral charge state defect as shown in Fig. 4(c). This starts the second, slower decay period of YL. During this period, the change of electron concentration n is relatively small, from initial $n = n_0 + N_D$ to final $n = n_0$, within a factor of 2. While, the concentration of neutral defect N_D^0 varies from N_D to zero. Thus, this period is almost an exponential, marked by the exponential decay of N_D^0.

Given the above picture, one can estimate the rough lifetime of the first decay. Note, this process is dominated by the RR_{BE}, but it is not a pure exponential since both n and p are decreasing. Nevertheless, we can estimate a characteristic time as $\tau_1^{YL} \approx {}^{1}/_{C_f(n_0 + 0.5(n_G + N_D))}$. The second decay is more pure, since the change of n is within a factor of 2 and the decay is mainly dominated by the decreasing of N_D^0. Thus we can estimate its lifetime as $\tau_2^{YL} \approx {}^{1}/_{C_n(n_0 + 0.5N_D)}$. The fast and slow decays of YL correspond to the decays of electron concentration n from $n_0 + n_G$ to $n_0 + N_D$ and then from $n_0 + N_D$ to n_0, respectively. The $n_0 + 0.5(n_G + N_D)$ and $n_0 + 0.5N_D$ in above expressions are the average electron concentrations $n(t)$ during these two periods. Due to the limitations of experimental instruments, previous works have reported only one of these two decays with one set of experimental measurements. This has contributed to the confusion in this field.

Since the defect concentrations of different samples vary greatly in the experiments, we next take a wide range of 5.0×10^{16} cm^{-3}-1.5×10^{18} cm^{-3} for the defect concentrations for a systematic study. The TRPL intensities of YL in different defect concentrations are shown in Fig. 5(a), and the corresponding fitted decay lifetimes are shown in Fig. 5(b). When the defect concentration ranges from 5.0×10^{16} cm^{-3} to 6.0×10^{17} cm^{-3}, as a result of the competition with the RR_{BE}, the shorter lifetimes of YL are maintained at the 10^{-10} s scales ($^{1}/_{C_f(n_0+0.5(n_G+N_D))}$), meanwhile, the long lifetimes of YL are all in the order of magnitude of microseconds due to its slow decay ($^{1}/_{C_n(n_0+0.5N_D)}$). In addition, both fast and slow decay lifetimes decrease slightly with the increase of N_D. However, when the defect concentration is 1.5×10^{18} cm^{-3}, as shown in Fig. 4(d), the time of the maximum point of RR_{YL} (5.9×10^{-11} s) precedes the cross point of RR_{BE} and RR_{YL} (4.4×10^{-11} s). At the maximum point of RR_{YL}, the RR_{BE} is an order of magnitude smaller than the RR_{YL}, and it will decrease exponentially. In those cases, the decay of YL is dominant, and YL only has a microsecond decay time as shown in Fig. 5(b).

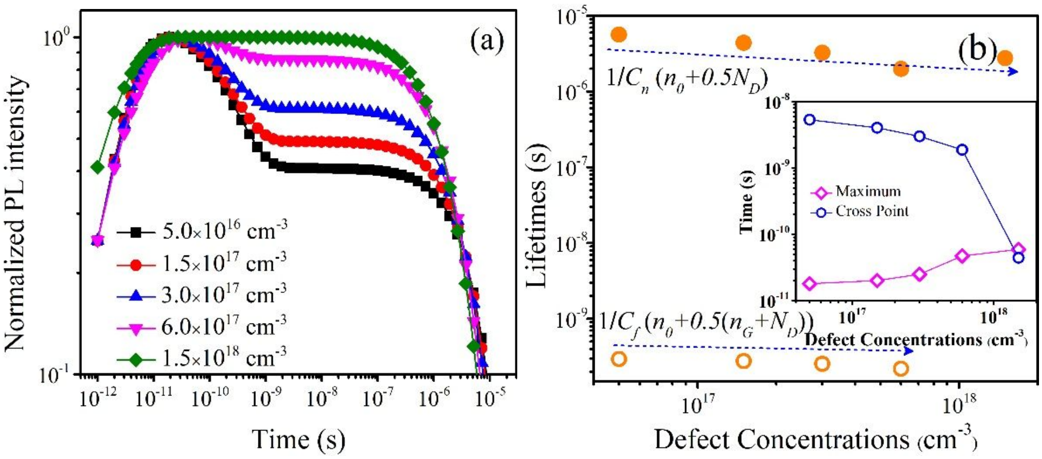

FIG. 5. The simulated decays of YL intensities when the defect concentrations are ranging from 5.0×10^{16} cm^{-3} to 1.5×10^{18} cm^{-3} (a), and the fitted decay lifetimes of YL at

different defect concentrations (b). The hollow and solid symbols in (b) are the fitted fast and slow lifetimes of YL. The time of the cross points of RR_{BE} and RR_{YL} curves and the maximum point of RR_{YL} at different defect concentrations as shown in the inset of Fig. 5(b).

Ⅳ. Experimental verification

In the TRPL experiment, a single instrument cannot simultaneously observe the decay lifetime of picosecond magnitude and microsecond magnitude. As a result, two sets of TRPL experiments were applied to verify the hundreds of picosecond and microsecond order of magnitude lifetime of YL in GaN that we just simulated. However, the same samples are used in these two experiments. The samples are carbon, silicon co-doped GaN film with a thickness of 2.6 μm grown on Si substrate by metal-organic chemical-vapor deposition (MOCVD). The concentration of intrinsic electron (n_0) measured by the Hall effect and the impurities (Si and C) concentrations measured by secondary ion mass spectrometry of two samples are listed in TABLE Ⅱ. The substitutional Si on the Ga site acts as a shallow donor, which is pretty well known[42]. We do not need to consider the shallow donor in our simulation. Incorporation of carbon impurity into GaN will form the substitutional defect C_N, rather than the complex defect C_N+O_N. This is proved by the fact the content of O in the sample is under the detection limit (2.0×10^{16} cm^{-3}).

In the first experiment, we used a laser emitting at 266 nm with a pulse width of about 180 fs and a repetition rate of 80 MHz. The average incident power is about 120 μW, and the diameter of the laser spot on the sample is about 4 μm. The resolution of the optical detection system is about 15 ps, and the detection range is about 4 ns. The measured TRPL intensities of YL are shown in Fig. 6(a) and show that YL intensities of the two samples both have picosecond magnitude decay. However, due to the experimental decay data of the two samples are very close and both have large noise, it is difficult to clearly distinguish the fast decay processes of the two samples. In the second experiment, the light source is a Xe-flash-lamp, emitting pulse of 2.5 μs duration at 280 nm with a repetition rate of 80 Hz. The average power of the exciting light on the surface of the sample is 32 mW, and the diameter of the light spot on the sample is about 5 mm in order to achieve a small injection. The resolution of the optical detection system is about 0.5 μs, and the detection range is about 0.1 ms. As shown in Fig. 6(b), the slow decay processes of YL of both samples are on the order of microseconds, and the double-exponential fitted decay lifetimes are 2.86×10^{-6} s, 2.33×10^{-5} s (for N-836) and 7.68×10^{-6} s, 3.51×10^{-5} s (for N-826), respectively. We think that the decay lifetimes of 2.33×10^{-5} s and 3.51×10^{-5} s are associated with other channels in the samples. By substituting the relevant parameters of the samples into the $\tau_2^{YL} \approx {}^{1}/_{C_n(n_0 + 0.5N_D)}$, we can estimate the simulated decay lifetimes of YL, which are 5.02×10^{-6} s (for N-836) and 6.59×10^{-6} s (for N-826) respectively. Our simulated decay lifetime of N-836 is about 1.8 times that of the experimental result, and the experimental slow decay lifetime of N-826 is about 1.2 times that of our simulated. However, both experimental and simulated decay lifetimes of N-836 are shorter than that of N-826, which is due to the intrinsic electron concentrations of sample N-836 being slightly higher than that of sample N-826, and their C impurity concentrations are similar. Fig. 5 shows that the shape of YL decay curves varies greatly with different defect concentrations, but even so, when the defect concentration is not higher than 1.5×10^{18} cm^{-3}, the simulated fast and slow decay lifetimes of YL will still maintain in the order of 10^{-10} s and 10^{-6} s magnitudes. In fact, some parameters used in our model are difficult to accurately measure in experiments, especially the concentrations of defect centers. This indicates that our simulated YL decay curves are difficult to completely accord with the experimental results, but the simulated fast and slow decay lifetimes are consistent with the experimental results in terms of magnitudes (10^{-10} s and 10^{-6} s).

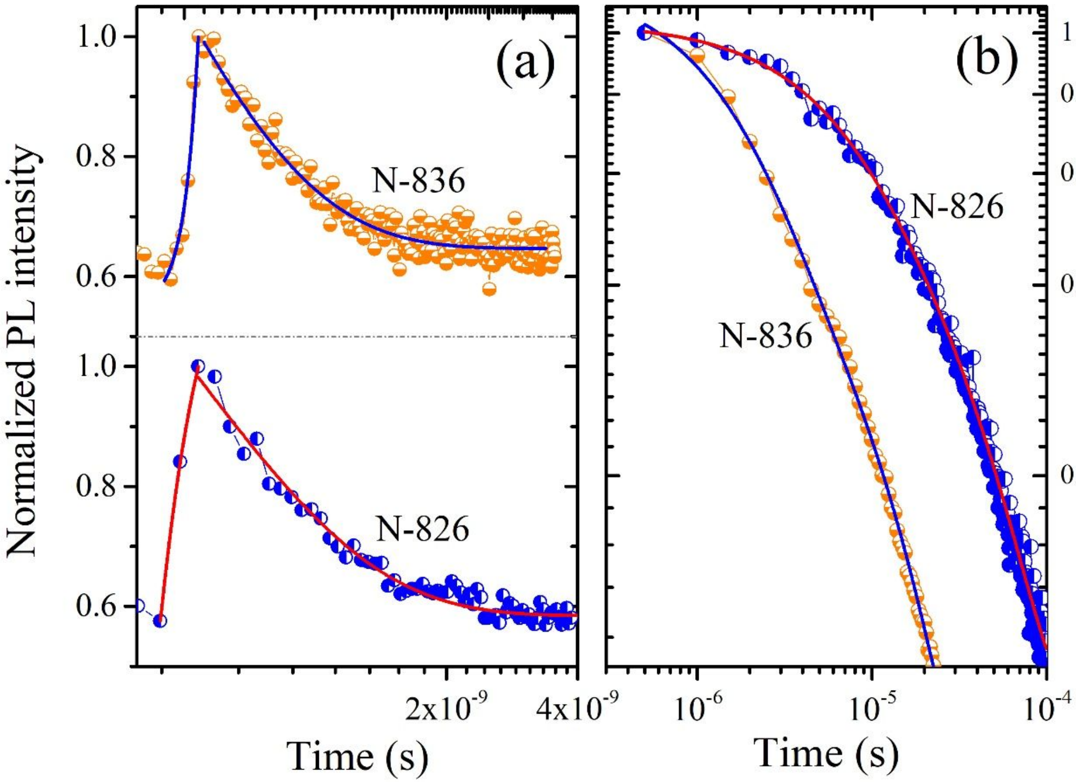

FIG. 6. The measured TRPL data of YL with the maximum at 2.20 eV in the first (a) and second (b) experiments. The blue and red solid lines in figure are the fitted data.

Since the YL of samples N-836 and N-826 have similar decay processes, we then only simulated the YL decay of sample N-836 and compared it with the experimental data. The corresponding parameters of first ($\lambda = 266$ nm, $a(\lambda) = 1.77\times10^{5}\,\mathrm{cm}^{-1}$, $I_0 = 4.34\times10^{7}\ \mathrm{W/cm^2}$) and second ($\lambda = 280$ nm, $\alpha(\lambda) = 1.62\times10^{5}\ \mathrm{cm}^{-3}$, $I_0 = 640\ \mathrm{W/cm^2}$) experiments are substituted into Eq. (1)-Eq. (4), we can get the time-resolved I_{YL}, and the results are shown in Fig. 7. The time steps in Fig. 7(a) and Fig. 7(b) are set to 15 ps and 0.5 μs to match the resolution in the experiments. Note, the carrier recombination during the laser pulse in the first experiment is ignored due to the pulse width is much faster than the carrier recombination. We know the measured fluorescence waveform is the convolution of the true decay profile with the IRF,[43] and the true YL decay curve of first experiment obtained by deconvolution is shown in Fig. 7(a). It should be note that, in order to avoid excessive noise, we first deconvolve the measured experimental data with the fitted IRF (red line in the inset of Fig. 7(a)) and then fit the deconvolved data. As one can see, the calculated results agree well with the experimental results. YL intensities will increase first and then exhibit a single exponential decay, and the fitted decay lifetimes of calculated and experimental curves are 2.39×10^{-10} s and 4.10×10^{-10} s, respectively. For the widely reported decay of YL on the order of microseconds, we do not deconvolve the measured experimental data with IRF, and the comparison between experimental and simulated slow decay curves of YL is shown in Fig. 7(b). It has been shown that, before about 5 μs, the calculated results agree very well with the experimental data. Whereas the experimental data decay slightly slower than the calculated results after 5 μs. This deviation at the long-timescale with a weak PL signal could be due to our model ignoring the consumption of electrons in the conduction band by the unknown recombination center. In the second experiment, our simulated decay lifetime is 3.94×10^{-6} s, which is consistent with the slower experimental decay lifetime of 2.86×10^{-6} s. Note, to highlight the decay of YL in the order of several hundred picoseconds and microseconds, the horizontal axis ranges of Fig. 7(a) and Fig. 7(b) are set to 500 ps and 9 μs, respectively.

The same sample shows very different experimental decay times at different regions of the time range, showing the double exponential nature of the TRPL, in agreement with our simulation. Obviously, neither of the above experiments is a good description of the whole YL decay process. Due to the limitation of the experimental setups, such as the measured time range, one separate experiment can only obtain partial characteristics of YL decay, but not the whole process. Our approach of combining direct *ab initio* simulation with experiment reveals the true characteristics and the mechanisms underneath the TRPL, representing a big step forward towards the understanding of the complex behavior of TRPL.

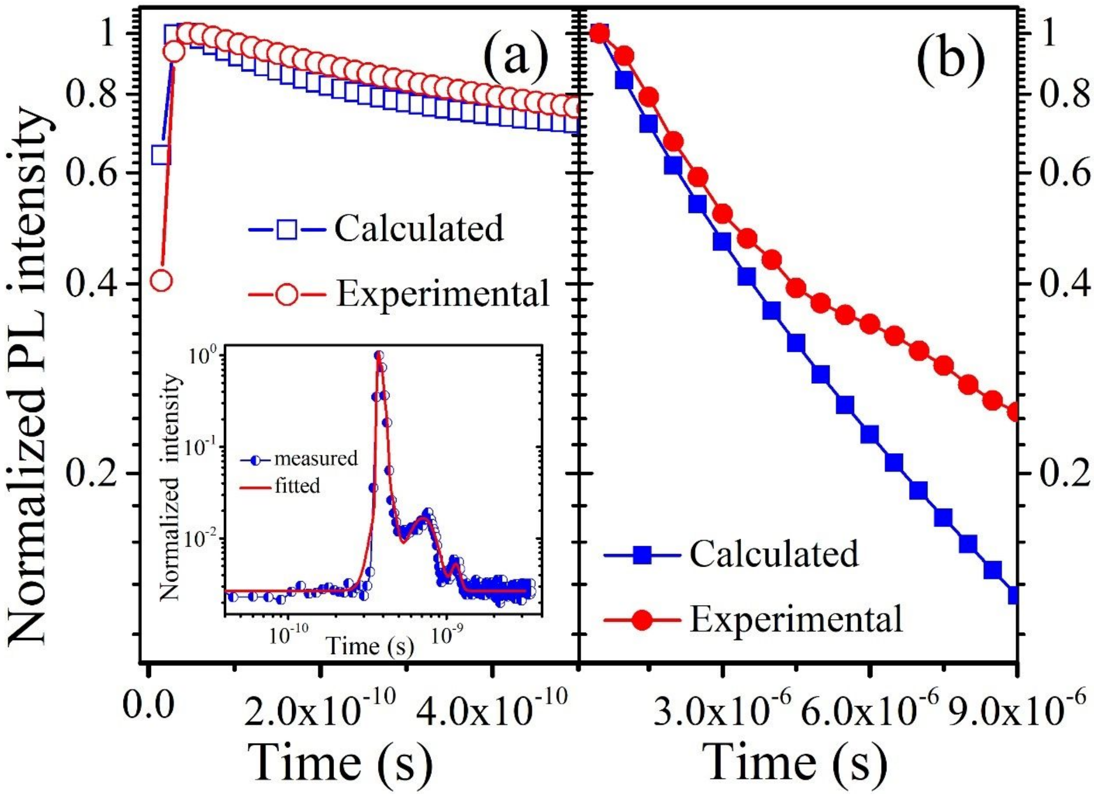

FIG. 7. The calculated in our model and experimental TRPL results of YL of sample N-836 for first (a) and second experiments (b). The hollow circles in (a) are the deconvolved results of the first experimental data, and the solid circles in (b) are the measured data of the second experiment. In the inset of Fig. 7(a), the blue symbols are the measured IRF data in first experiment, and the red line is the fitted IRF data. Both (a) and (b), we align the time of the maximum of experimental and calculated YL intensities.

Ⅴ. Conclusion

In summary, we propose a theoretical model that can describe the deep impurity levels related TRPL process in WBGS based on SRH model, and the dynamic competition of different recombination channels. Combining theoretical simulation and experimental measurement, we reveal the mechanism of the YL TRPL decay, which is caused by the electron transition from the conduction band edge to the C_N^0 defect center. We propose that in the case of large injection, the initial fast decay in the first hundreds of picoseconds is caused by the reduction of the band edge electron concentration *n*, while the concentration of C_N^0 is more or less constant due to fast hole pumping to the defect center from the valence band edge. The reduction of *n* is mostly caused by band edge emission. The slow decay in the order of μs is due to the slow decay of the concentration of C_N^0 defect caused by electron transition from the conduction band to C_N^0 defect. During this time, the band edge hole concentration has been depleted. In addition, we compare the decay of YL when the defect concentration varies from 5.0×10^{16} cm^{-3} to 1.5×10^{18} cm^{-3}. When the defect concentration is 1.5×10^{18} cm^{-3}, slightly higher than the photo-generated carriers, the YL recombination channel will dominate over the direct band-edge recombination channel. As a consequence, YL will only have one μs decay lifetime. We think our method provides an important support to explain the experimental TRPL. It also leads to a better understanding of the competition between deep level recombination channels in WBGS. Our quantitative agreements between theory and experiment further confirm the accuracy of our theoretically calculated recombination rates for different channels.

Author Contributions

H. S. Zhang: Conceptualization, Data curation, Investigation, Methodology, Software, Visualization, Writing-original draft. L. Shi: Conceptualization, Funding acquisition, Supervision, Investigation, Methodology, Software, Writing-review & editing. Z. H. Liu: Resources, Validation. G. Z. Xu: Resources, Validation. W. T. Song: Resources, Validation. Y. K. Wang: Validation. Z. J. Xu: Software. X. B. Yang: Funding acquisition. Y. J. Zhao: Funding acquisition. X. L. Yang: Resources. B. Shen: Resources. L. W. Wang: Supervision, Writing-review & editing. K. Xu: Resources, Supervision.

Conflict of Interest

The authors declare no conflict of interest.

Acknowledgements

H. S. Zhang is supported by the Youth Program of National Natural Science Foundation of China (Grant No. 12004204), the Natural Science Foundation of Inner Mongolia Autonomous Region (Grant No. 2020BS01003) and the GHfund B (20210702). L.S. is supported by the National Natural Science Foundation of China (Grant No. 11374328), the National Key Research and Development Program of China (Grant No. 2016YFA0201101, 2016YFE0105700), the National Science Fund for Distinguished Young Scholars (Grant No. 61325022), the Youth Innovation Promotion Association Chinese Academy of Science (CAS) (Grant No. 2016289), and the Foundation of

Suzhou Institute of Nano-Tech and Nano-Bionics (SINANO) (Grant No. Y5AAC11001). Wang is supported by the Director, Office of Science, the Office of Basic Energy Sciences (BES), Materials Sciences and Engineering (MSE) Division of the U.S. Department of Energy (DOE) through the theory of material (KC2301) program under Contract No. DEAC02-05CH11231. We are grateful for the professional services offered by the Platforms of Characterization & Test at SINANO, and Supercomputing Center, CNIC, CAS.

TABLE I. Parameters of GaN samples analyzed in this paper. The recombination coefficients C_f, C_n and C_p are cited from our previous work[25].

C_f (cm^{-3}s^{-1})	C_p (cm^{-3}s^{-1})	C_n (cm^{-3}s^{-1})	n_0 (cm^{-3})	N_D (cm^{-3})
4.24×10^{-9}	2.67×10^{-7}	3.16×10^{-13}	4.50×10^{17}	3.60×10^{17}

TABLE Ⅱ. Parameters of GaN samples analyzed in this paper.

Sample number	[C] from SIMS(cm^{-3})	[Si] from SIMS(cm^{-3})	n_0 at 300 K (cm^{-3})
N-836	~7.0×10^{17}	1.9×10^{18}	4.5×10^{17}
N-826	~7.0×10^{17}	1.0×10^{18}	3.0×10^{17}

REFERENCES

1 J. Narvaez, F. Vasquez-Sancho and G. Catalan, *Nature*, 2016, **538**, 219-221.

2 X. Duan, Y. Huang, Y. Cui, J. Wang and C. M. Lieber, *Nature*, 2001, **409**, 66-69.

3 K. Tomioka, M. Yoshimura and T. Fukui, *Nature*, 2012, **488**, 189-192.

4 X. Ming, X. Duan, J. Zhang and H. Yue, *IEEE Electr Device Lett.*, 2018, **PP**, 1-1.

5 D. V. Lang, *J. Appl. Phys.*, 1974, **45**, 3023-3032.

6 I.-H. Lee, A. Y. Polyakov, N. B. Smirnov, A. V. Govorkov, A. S. Usikov, H. Helava, Y. N. Makarov and S. J. Pearton, *J. Appl. Phys.*, 2014, **115**, 223702.

7 K. Saarinen, P. Seppälä, J. Oila, P. Hautojärvi, C. Corbel, O. Briot and R. L. Aulombard, *Appl. Phys. Lett.*, 1998, **73**, 3253-3255.

8 S. Paudel, M. E. Zvanut, M. Iwinska, T. Sochacki and M. Bockowski, *Physica Status Solidi (b)*, 2019, **257/4**, 1900593.

9 D. M. Hofmann, D. Kovalev, G. Steude, B. K. Meyer, A. Hoffmann, L. Eckey, R. Heitz, T. Detchprom, H. Amano and I. Akasaki, *Phys. Rev. B*, 1995, **52**, 16702-16706.

10 D. O. Demchenko, I. C. Diallo and M. A. Reshchikov, *Phys. Rev. Lett.*, 2013, **110**, 087404.

11 M. A. Reshchikov, D. O. Demchenko, J. D. McNamara, S. Fernández-Garrido and R. Calarco, *Phys. Rev. B*, 2014, **90**, 035207.

12 S. Albert, A. E. Bragg and D. M. Neumark, *Cheminform*, 2004, **35**, 1719-1757.

13 H. Haag, B. Hönerlage, O. Briot and R. L. Aulombard, *Phys. Rev. B*, 1999, **60**, 11624-11630.

14 C. Díaz-Guerra, J. Piqueras and A. Cavallini, *Appl. Phys. Lett.*, 2003, **82**, 2050-2052.

15 D. G. Chtchekine, L. P. Fu, G. D. Gilliland, Y. Chen, S. E. Ralph, K. K. Bajaj, Y. Bu, M. C. Lin, F. T. Bacalzo and S. R. Stock, *J. Appl. Phys.*, 1997, **81**, 2197-2207.

16 R. Y. Korotkov, M. A. Reshchikov and B. W. Wessels, *Physica B*, 2003, **325**, 1-7.

17 J. Mickevicius, G. Tamulaitis, P. Vitta, A. Zukauskas, M. S. Shur, J. Zhang, J. Yang and R. Gaska, *Solid State Commun.*, 2008, **145**, 312-315.

18 M. A. Reshchikov, *J. Appl. Phys.*, 2014, **115**, 103503.

19 M. A. Reshchikov, J. D. Mcnamara, M. Toporkov, V. Avrutin, H. Morkoç, A. Usikov, H. Helava and Y. Makarov, *Sci. Rep.*, 2016, **6**, 37511.

20 M. A. Reshchikov, R. M. Sayeed, Ü. Özgür, D. O. Demchenko, J. D. McNamara, V. Prozheeva, F. Tuomisto, H. Helava, A. Usikov and Y. Makarov, *Phys. Rev. B*, 2019, **100**, 045204.

21 M. A. Reshchikov, *J. Appl. Phys.*, 2021, **129**, 121101.

22 J. Heyd, G. E. Scuseria and M. Ernzerhof, *J. Chem. Phys*., 2003, **118**, 8207-8215.

23 J. Heyd, G. E. Scuseria and M. Ernzerhof, *J. Chem. Phys*., 2006, **124**, 219906.

24 J. L. Lyons, A. Janotti and C. G. Van de Walle, *Appl. Phys. Lett.*, 2010, **97**, 152108.

25 H. S. Zhang, L. Shi, X. B. Yang, Y. J. Zhao, K. Xu and L. W. Wang, *Adv. Opt. Mater.*, 2017, **5**, 1700404.

26 L. Shi and L.-W. Wang, *Phys. Rev. Lett.*, 2012, **109**, 245501.

27 A. Alkauskas, Q. Yan and C. G. Van de Walle, *Phys. Rev. B*, 2014, **90**, 075202.

28 L. Shi, K. Xu and L.-W. Wang, *Phys. Rev. B*, 2015, **91**, 205315.

29 W. Jia, Z. Cao, L. Wang, J. Fu, X. Chi, W. Gao and L.-W. Wang, *Comput. Phys. Commun.*, 2013, **184**, 9-18.

30 W. Jia, J. Fu, Z. Cao, L. Wang, X. Chi, W. Gao and L.-W. Wang, *J. Comput. Phys.*, 2013, **251**, 102-115.

31 G. I. B. Henderson, *Optical Spectroscopy of Inorganic Solids*, Clarendon, Oxford, UK, 1989.

32 A. F. van Driel, G. Allan, C. Delerue, P. Lodahl, W. L. Vos and D. Vanmaekelbergh, *Phys. Rev. Lett.*, 2005, **95**, 236804.

33 Y. Tokuda, *ECS Transactions*, 2016, **75**, 39-49.

34 S. Wu, X. Yang, H. Zhang, L. Shi, Q. Zhang, Q. Shang, Z. Qi, Y. Xu, J. Zhang, N. Tang, X. Wang, W. Ge, K. Xu and B. Shen, *Phys. Rev. Lett.*, 2018, **121**, 145505.

35 G. Kresse and J. Furthmüller, *Phys. Rev. B*, 1996, **54**, 11169.

36 G. Kresse and D. Joubert, *Phys. Rev. B*, 1999, **59**, 1758-1775.

37 W. Shockley and W. T. Read, *Phys. Rev.*, 1952, **87**, 835-842.

38 M. A. Reshchikov and R. Y. Korotkov, *Phys. Rev. B*, 2001, **64**, 115205.

39 J.-H. Yang, L. Shi, L.-W. Wang and S.-H. Wei, *Sci. Rep.*, 2016, **6**, 21712.

40 J. F. Muth, J. H. Lee, I. K. Shmagin, R. M. Kolbas, H. C. Casey, B. P. Keller, U. K. Mishra and S. P. DenBaars, *Appl. Phys. Lett.*, 1997, **71**, 2572-2574.

41 K. Kumakura, T. Makimoto, N. Kobayashi, T. Hashizume, T. Fukui and H. Hasegawa, *Appl. Phys. Lett.*, 2005, **86**, 380.

42 S. Nakamura and G. Fosol, *The Blue Laser Diode*, Springer, Berlin, 1998.

43 W. Becker, *The bh TCSPC Handbook*, 7th edn., 2017.